Imaging heterogeneous 3D dynamics of individual solutes in a polyelectrolyte brush

Dongyu Fan[1], Shahryar Ramezani Bajgiran[1], Farshad Safi Samghabadi[2], Chayan Dutta[3], Emil Gillett[4], Peter J. Rossky*[1,4,6], Jacinta C. Conrad*[2], Amanda B. Marciel*[1], Christy F. Landes*[1,4,5,6]

[1]Department of Chemical and Biomolecular Engineering, Rice University, Houston, TX, USA, 77005

[2]Department of Chemical and Biomolecular Engineering, University of Houston, Houston, TX, USA, 77204

[3]Department of Chemistry, Georgia State University, Atlanta, GA, USA, 30302

[4]Department of Chemistry, Rice University, Houston, TX, USA, 77005

[5]Department of Electrical and Computer Engineering, Rice University, Houston, TX, USA, 77005

[6]Smalley Curl Institute, Rice University, Houston, TX, USA, 77005

To whom correspondence should be addressed: Christy F. Landes cflandes@rice.edu

Abstract

Understanding molecular transport in polyelectrolyte brushes (PEBs) is crucial for applications such as separations, drug delivery, anti-fouling, and biosensors, where structural features of the polymer control intermolecular interactions. The complex structure and local heterogeneity of PEBs, while theoretically predicated, are not easily accessed with conventional experimental methods. In this work, we use 3D single-molecule tracking to understand transport behavior within a cationic poly(2-(N, N-dimethylamino)ethyl acrylate) (PDMAEA) brush using an anionic dye, Alexa Fluor 546, as the probe. The analysis is done by a parallelized, unbiased 3D tracking algorithm. Our results explicitly demonstrate that spatial heterogeneity within the brush manifests as heterogeneity of single-molecule displacements. Two distinct populations of probe motion are identified, with anticorrelated axial and lateral transport confinement, which we believe to correspond to intra- vs. inter-chain probe motion.

Introduction

Polyelectrolyte brushes (PEBs) are charged polymers that have one end covalently tethered to a surface with the other end extending into the medium.[1] The unique properties resulting from the extended polymer conformation and the tunable behavior of the charged polymer moieties[2] underpin applications of PEBs in drug delivery,[3] bio-sensing,[4] antibacterial coatings,[5] and biomolecular separations.[6] In most applications, molecules and nanoscale particles interact or diffuse on or inside the brush layer, which calls for a deeper molecular-scale understanding of the structure and its relation to transport mechanisms inside the PEBs.

The complex structure of PEBs adds to the difficulty of investigating transport mechanisms inside the brush architecture. Weak PEBs switch between collapsed and swollen states in response to pH changes[7], and polyelectrolytes more generally are sensitive to environmental ionic strength.[2, 8] Scaling arguments and Self-Consistent Field Theory (SCFT) have been used to model the conformation of PEBs.[9] The monomer volume fraction (φ) is predicted to be non-uniform inside a PEB in a normal direction from the surface, with an extended parabolic profile. Also, the local degree of ionization of polyelectrolytes depends on φ, varying with the distance from the substrate.[10,11] Ensemble-averaged experimental methods have been successfully used to verify the predicted φ profiles and charge distribution within PEBs.[12,13,14] However, these methods fail to give a local, molecular-level understanding of the heterogeneities inside PEBs.

Fluorescence microscopy can provide insight into transport mechanisms within polymer brushes. Techniques such as fluorescence correlation spectroscopy (FCS) are widely used to study motion in complex structures[15]. Studies applying FCS found molecule motion in a polymer brush is controlled by grafting density,[16,17], as well as structural change and solution ionic strength in a charged system[18]. Other than fluorophore motion, orientation can also be monitored with polarization-resolved FCS,[19], whereas the effect of flow velocity is explored with the Förster resonance energy transfer (FRET) method[20]. However, these methods provide only indirect access to the brush's local structural heterogeneity.

Single-molecule tracking offers the ability to monitor different transport mechanisms inside and near the brush surface,[21, 22, 23] and single-molecule localization has been applied to resolve polymer conformation.[24] 3D single-molecule localization is enabled by phase engineering,[25] with axial information of the single fluorophores encoded in the shape of a double helix point spread function (DH-PSF) accessed in a 2D image. Wöll's group utilized 3D single-molecule imaging to resolve the complex structure inside stimuli-responsive polymer networks.[26] This technique was recently extended and optimized for high-precision tracking with the unbiased tracking algorithm Knowing Nothing Outside Tracking (KNOT).[27] KNOT can provide precise tracking at a cost of low computational efficiency. Because gathering detailed insight into transport in complex structures requires large data sets, high throughput analysis methods that implement parallel high-performance computing (HPC) algorithms[28] are necessary.

In this study, we perform 3D single-molecule tracking of the anionic dye molecule Alexa Fluor 546 in a poly-(2-(N, N-dimethylamino)ethyl acrylate) (PDMAEA) cationic brush,

which is protonated and swollen as long as the local pH is lower than the effective brush local pKa. To process the tracking data with high throughput, we employed parallel computing with an HPC cluster on a 3D single-molecule tracking algorithm. Two different transport processes are observed inside the swollen PDMAEA brush, revealing significant spatial heterogeneity within the brush. This approach can be widely applied to study molecule transport in complex systems.

Methods

Initiator deposition. Plasma-cleaned microscope coverslips (cleaning procedure described in Supporting Information, section 1) and silicon substrates (Addison Engineering) are placed inside a vacuum chamber alongside a vial containing 100 μL of 3-(aminopropyl) triethoxysilane (APTES, 99%, Sigma-Aldrich), and the vacuum is pulled for 4 min. The chamber is then detached from the vacuum line and left to react for 1.5 h under a static vacuum. The APTES-modified substrates are collected from the chamber and annealed under vacuum at 110°C for 1 h. The annealed substrates are then transferred into a glove box operating under an argon atmosphere. APTES-modified substrates are placed in a glass petri dish containing 12 mL of tetrahydrofuran (THF, anhydrous, Sigma-Aldrich). Triethylamine (TEA, 99.5%, Sigma-Aldrich) is then added to the solution (0.55 mL, 0.3 M) followed by the dropwise addition of α-bromoisobutyryl bromide (BiBB, 98%, Sigma-Aldrich) (0.5 mL, 0.3 M). After 1.5 h, the substrates are removed and washed with copious amounts of THF, methanol (ACS grade, Sigma-Aldrich), and water and then dried under a nitrogen stream. (A

schematic of this process is shown in Figure S1.) X-ray photoelectron spectroscopy (XPS) is used to verify APTES-BiBB initiator attachment to surfaces (Figure S2).

Polymer brush synthesis. Surface-initiated copper(0) radical polymerization (SI-CuCRP) is used to synthesize PEBs, where a copper(0) plate is used as the catalyst source.[29, 30, 31] Copper plates are sonicated in dimethyl sulfoxide (DMSO, ACS grade, Sigma-Aldrich) and methanol to remove the oxide layer, then dried under nitrogen flow and used immediately for the synthesis. PDMS spacers (thickness = 0.5 mm) are sandwiched between the initiator-modified substrates and copper plates. The sandwiched setup is then placed in a custom-made reaction vessel to minimize the required volume and prevent the evaporation of the reaction mixture. The reaction solution is prepared by adding 2-(dimethylamino)ethyl acrylate (DMAEA, 98%, Sigma-Aldrich) (1.25 M) to a water/methanol solvent mixture (2:1 (v/v)), followed by N, N, N', N", N"-pentamethyldiethylenetriamine (PMDETA, 99%, Sigma-Aldrich) (40 mM) as the ligand and stirred until homogeneous. Next, a small amount (1.5 mL for 22 × 22 mm^2 and 4 mL for 25 × 75 mm^2) of the reaction solution is injected into the reaction vessel. The vessels are capped and left to react at room temperature for 0.5 h. Polymerization is terminated by removing the copper plate from the setup. Coverslips and silicon pieces are rinsed with acetone, methanol, and water, and then sonicated in methanol and water, dried under a gentle nitrogen stream, and stored in a dry environment. Ellipsometry and atomic force microscopy (AFM) are used to determine brush thickness and surface roughness (Figure S3).

Fluorescent dye solutions. Probe solutions are prepared by diluting Alexa Fluor 546 carboxylic acid (Tris(triethylammonium) salt, Life Technologies) to 5 pM in molecular

biology grade water (pH 5.7, Thermo Scientific) and hydrochloric acid (HCl, Fisher Chemical) solution with a pH of 3.

Ellipsometry. Brush thickness under wet and dry conditions is measured using an ellipsometer (M-2000S, J.A. Woollam). For dry measurements, clean samples are measured at three angles (65, 70, and 75°) and the spectra are analyzed using WVASE32 software. Data are fit with a Cauchy model, $n(\lambda) = A + B/\lambda^2$, for brush thickness and the first two Cauchy parameters, A and B. Wet measurements are performed using a liquid cell (J.A. Woollam) with a fixed nominal angle of incidence of 75° and a volume of 5 mL. To ensure steady-state conditions inside the cell, a 50 mL exchange volume and 30 min equilibration time are used. To analyze *in-situ* ellipsometry results, a graded layer model in combination with an effective medium approach (EMA) is used. In this model,[32] the PEB is divided into two main layers with each layer sliced into five sublayers. The Cauchy parameters obtained from dry measurements are set as constants and data are fit for brush thickness, middle node position, and polyelectrolyte fraction in EMA layers.

Microscope. Imaging is performed using a home-built fluorescence microscope with a 560 nm green laser from a white light laser (SuperK FIANIUM) operating at a 78 MHz repetition rate. The excitation light is collimated onto the sample with a high numerical aperture oil-immersion objective (100x magnification, NA = 1.46, Carl-Zeiss, alpha Plan-Apochromat). The emitted light is collected in epifluorescence mode, passing through the same objective, filtered by a Chroma z532/633rpc dichroic mirror, and focused at a tube lens with f = 165 mm. Finally, the signal passes through a 4f system consisting of two lenses with a Double Helix (DH) phase mask (Double Helix LLC)[25], and the image is recorded by a

back-illuminated sCMOS camera (Photometrics Prime 95B, 600×600 pixel area, 68.5 nm pixel size).

Single-molecule measurements. Microscope coverslips grafted with PEBs are covered with a custom flow chamber (Grace Bio-Labs). Tubing (Scientific Commodities, 0.03" internal diameter) is connected to the chamber with inlet and outlet flow controlled by a syringe pump (Genie Plus, Kent Scientific) (Figure 1a). At a given pH, 50 μL of buffer solution is flowed into the chamber at a volumetric rate of 50 μL/min. Next, the dye solution is flowed in at the same flow rate and is allowed to equilibrate for 15 min. After equilibration, movies containing 1000 images are recorded at 20 fps. The recorded motion of dye molecules is analyzed with an unbiased tracking algorithm.[27] (Details are discussed in Results and Discussion.)

Trajectory Analysis. The radius of gyration (R_g) of a particle trajectory is generated from the corresponding set of positions and quantifies the volume that a particle explores and its mobility.[33] The 3D radius of gyration is determined from the eigenvalues of the tensor, where x,y, and z represent the x,y, and z coordinates of a particle, respectively.

$$\hat{T} = \frac{1}{N}\begin{pmatrix} \sum_{j=1}^{N}(x_j - \langle x\rangle)^2 & \sum_{j=1}^{N}(x_j - \langle x\rangle)(y_j - \langle y\rangle) & \sum_{j=1}^{N}(x_j - \langle x\rangle)(z_j - \langle z\rangle) \\ \sum_{j=1}^{N}(x_j - \langle x\rangle)(y_j - \langle y\rangle) & \sum_{j=1}^{N}(y_j - \langle y\rangle)^2 & \sum_{j=1}^{N}(y_j - \langle y\rangle)(z_j - \langle z\rangle) \\ \sum_{j=1}^{N}(x_j - \langle x\rangle)(z_j - \langle z\rangle) & \sum_{j=1}^{N}(y_j - \langle y\rangle)(z_j - \langle z\rangle) & \sum_{j=1}^{N}(z_j - \langle z\rangle)^2 \end{pmatrix}$$

The scalar radius of gyration R_g is the root mean square of the three eigenvalues R_i of $\hat{T}$, i.e. $R_g = \sqrt{R_1^2 + R_2^2 + R_3^2}$.

The dynamic character of the probes is investigated via mean square displacement (MSD) anlaysis.[34]

Results and Discussion

3D tracking of charged dye molecules using phase engineering enables dynamic information about transport in weak PEBs. The schematics for the microscope and the microfluidic sample chamber are shown in Figure 1a. We use a microfluidic setup to control the pH and probe concentrations throughout the measurement. A 4f beam geometry with a phase mask inserted in the Fourier plane encodes 3D information of the point emitters into the DH-PSF.[25] The inset cartoon illustrates the side view of dye molecules interacting with a polymer brush at various depths of the brush. Molecular structures of the anionic Alexa Fluor 546 dye and PDMAEA brush are depicted in Figures 1b and c, respectively. PDMAEA brush chemistry, conformation, and thickness can be tuned through solution conditions. The ionization behavior of weak PEBs is dependent on the effective

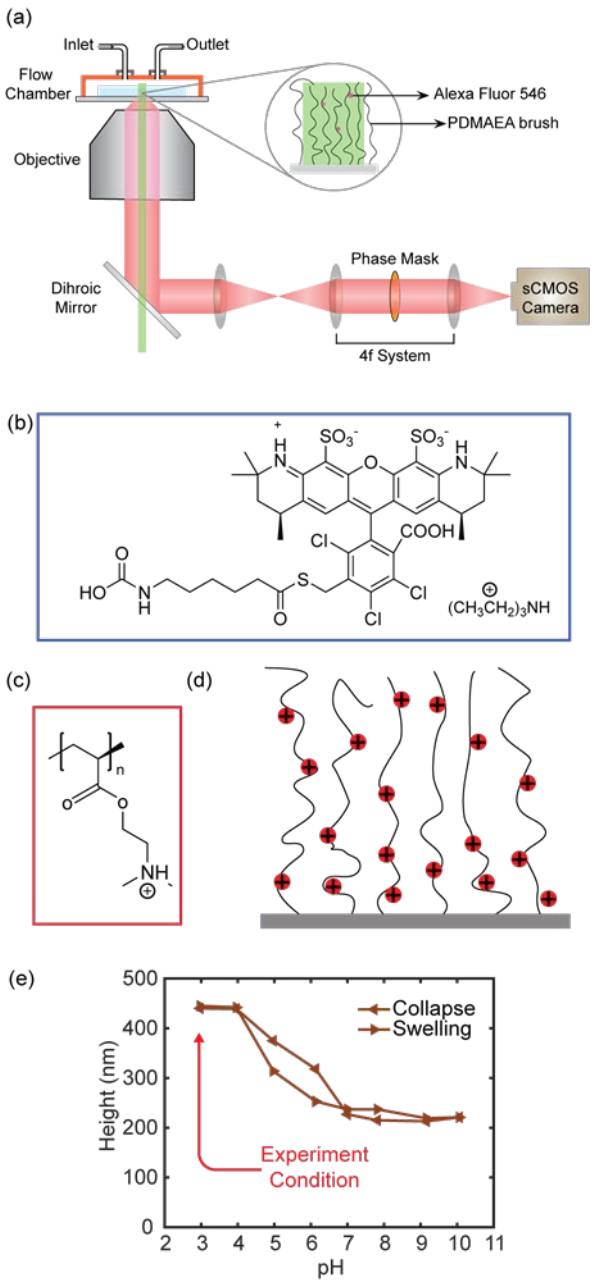

Figure 1: Phase engineering enables 3D tracking of charged dyes in a tunable weak poly-cationic brush. (a) Schematic of the microscope and flow system. The inset cartoon illustrates the side view of dye molecules interacting with polymer brushes. (b, c) Molecule structure of (b) Alexa Fluor 546, negatively charged (blue box), and (c) PDMAEA, positively charged (red box). (d) A cartoon representation (side view) of the conformation of PDMAEA brushes at a fully changed state. (e) Wet ellipsometry measurement of PDMAEA brush height as a function of pH.

brush pKa and the local proton concentration in the brush[10,35,36]. The effective pKa of the PDMAEA brush shifts from the monomer pKa of 8.3[37] to lower pH values due to electrostatic repulsions along the chains[38]. For pH values below the effective pKa, the PDMAEA brush is fully charged due to protonation of the tertiary amine groups. A cartoon representation (side view) of this state is depicted in Figure 1d. At this condition, the brush swells to the maximum height due to electrostatic repulsion between the polyelectrolyte chains. As the pH is increased, the amine groups become deprotonated and the brush starts to collapse, leading to a change in the brush height determined with *in-situ* wet ellipsometry (Figure 1e). The effective pKa in this experiment is shown to be around 5-6 with hysteresis effect making it difficult to determine the exact value.

In this study, we fix the experimental pH value at 3, where the brush is unambiguously at maximum height (see Fig. 1e), to understand brush heterogeneity at this extreme of charge and extension. Raw movies of Alexa motion inside PDMAEA brushes at pH 3 and other conditions are included in the Supporting Information. The single-molecule motions with phase-engineered PSFs are recorded as movies and analyzed by an unbiased tracking algorithm KNOT.[27] Control tracking data show that the probe transport behavior at other pH conditions becomes even more complex than is discussed in the current study (details are shown in the Supporting Information, section 3). We restrict the current analysis and discussion to the fully ionized brush condition to demonstrate that in even this simplest case, local brush heterogeneity can lead to strongly different local solute dynamics.

Parallel computing on the HPC cluster accelerates KNOT computation time and makes it possible to track thousands of dye trajectories. The KNOT algorithm takes four steps to form particle trajectories, among which the point cloud representation is the most time-consuming (Figure 2a). In this step, the Alternating Direction Method of Multiplier (ADMM) is used to recover the particle positions, represented by a point cloud.[27] For every frame, ADMM independently generates a set of point clouds that converge on possible particle positions with hundreds of iterations. While performing well on complex phase-engineered single-molecule PSFs, the low computational efficiency becomes a choke point in data analysis.

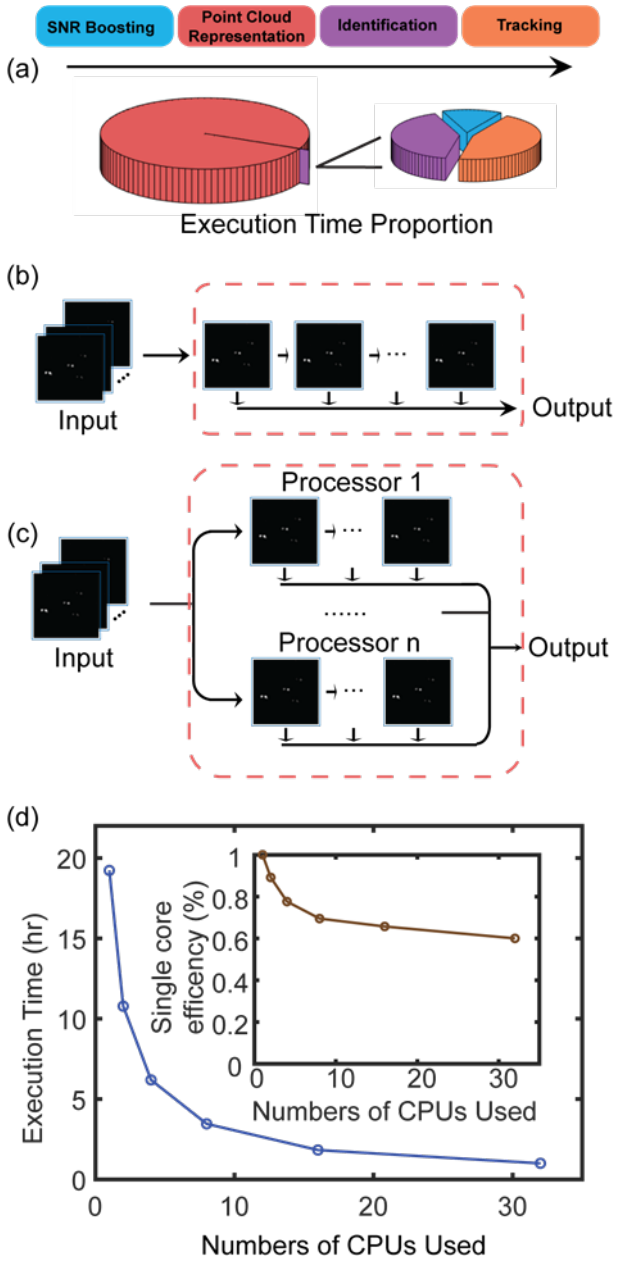

Figure 2: Parallel computing accelerates KNOT computation time. (a) A schematic of the KNOT work flow and an illustration of the execution time proportion for each step. (b, c) Workflow of single string (b) and parallelized (c) deconvolution process. (d) Execution time and single core efficiency (inserted) decreases as a function of the number of CPUs used.

Applying parallel computing on the point cloud representation step shortens the computational time. Using one processor, this program performs ADMM[39] sequentially on every frame (Figure 2b). By parallelizing this process, it is possible to distribute the different frames to multiple processors with the *multiprocessing* package (Figure 2c). An HPC cluster provides numerous high-performance CPUs for this paralleling computing process and the computational time decreases by increasing CPU numbers (Figure 2d). The single-core efficiency also decreases slightly with the CPU number (Figure 2d, inset), which we believe is due to the uneven distribution of tasks onto different cores. Depending on the available resources in the cluster, multiple datasets may be processed simultaneously to achieve high throughput data processing. The particle trajectories are then formed using single-frame displacement analysis with our unbiased tracking algorithm.[27]

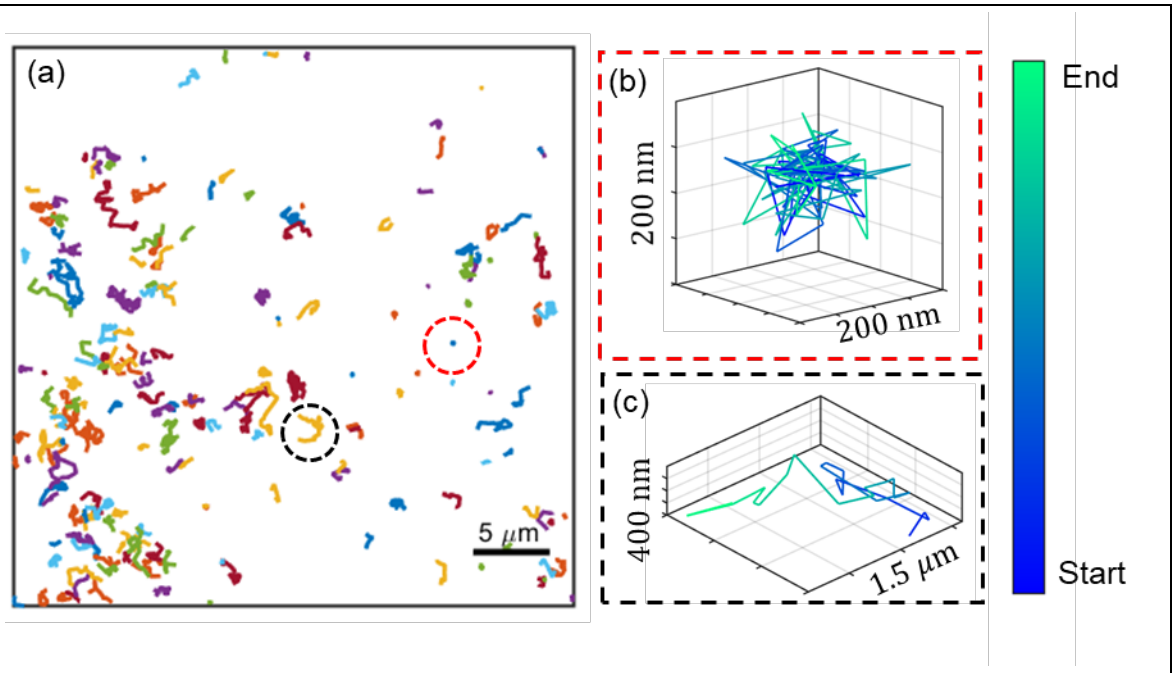

Figure 3: Confined and unconfined probe motions are observed in the brush at pH 3. (a) 2D projection of 200 randomly selected trajectories of an Alexa 546 dye probe measured in the same region in a PDMAEA brush. Colors indicate different trajectories. (b-c) 3D view of two illustrative trajectories circled in (a), representing confined (red) and unconfined motion (black), respectively.

Two distinct types of dye motion in the brush are observed at pH 3. Using the parallelized algorithm, we tracked over 8000 probe trajectories within the same region ($34 \times 34\ \mu m$) of a swollen PDMAEA brush at pH 3, with 200 randomly selected trajectories shown in Figure 3a as a 2D projection. Here, it is possible to recognize spatially heterogeneous dynamics; both confined probes (red circle) and probes that are exploring their local brush regions by unconfined motion are evident (black circle). Two illustrative trajectories with full 3D information further reveal that a confined probe exhibits restricted motion in all three dimensions (Figure 3b), whereas an unconfined probe with larger mobility in-plane appears to have limited motion in the z direction in the observable time scale (Figure 3c). (Details discussed in Figure S4, Supporting Information.) In addition to these types of motion, previous studies have also reported the adsorption/desorption of positively charged

Rhodamine 6G in an oppositely charged strong polyanionic brush (sodium poly(styrene sulfonate)) within ~250 nm detection range at millisecond time scales.[40] Given the localization precision of ~ 20 nm in plane and ~ 30 nm in axial in our experiments,[27] and the relatively large length dimensions observed for confined motion (200 nm), we see no evidence of adsorptive behavior in our experiments.

The dynamics of probes in the PDMAEA brush can be affected by the local brush properties, including polymer density and the electrostatic potential, which both vary as a function of distance normal to the surface. The grafting density of our PDMAEA brush is 0.25 chains/nm^2 leading to an average distance of 2 nm between chains near the substrate (measurement details are provided in Supporting Information, section 5). The hydrodynamic radius of Alexa Fluor 546 is about 0.66 nm, calculated from its reported free diffusion coefficient in water.[41] Thus, we believe the confined population represents probes that are interacting with regions of higher local polymer chain density and, correspondingly, more negative local electrostatic potential, as would occur if the probe interacted with more than one nearby (oppositely) charged polymer simultaneously. Such a deepening of the potential well via multiple stabilizing interactions extends the residence time in a confined state by raising the free energy barrier for release from the well to a more mobile state[42].

There are large local differences in probe dynamics, which suggests that microscale brush heterogeneity persists even at pH = 3, when the brush should be maximally swollen. The transport of probes, characterized by R_g, which accounts for the displacement of every point in a trajectory from the initial particle position, is location-dependent. Figure 4 shows a heatmap of the weighted average value of R_g on a log scale in a representative region, measured at pH 3 with the maximum field of view. Heat maps with decreasing grid sizes were plotted and a grid length of 1 μm was chosen as the smallest grid size that mapped the local R_g with sufficient data density (Figure S5). The dark grids represent regions where the probes are confined, whereas the brighter grids indicate regions where the probes are more mobile. The blank grid areas show regions in which no probe is detected.

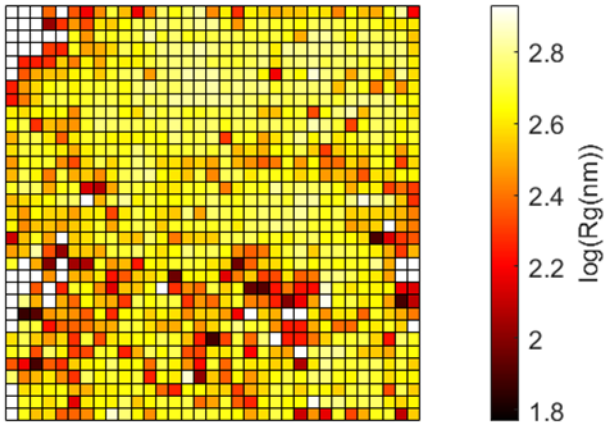

Figure 4 PDMAEA brush presents spatial heterogeneity. 8102 trajectories are collected at the same region of the brush. The heatmap represents the weighted average value of the trajectory's radius of gyration in that region. One grid corresponds to a length of 1μm.

The probe R_g depends on location in the brush on the micron scale. This result supports a model in which regions with smaller R_g have higher polymer density with stronger electrostatic attraction to the probes due to excess electrostatic potential inside the brush that localizes probes[43]. The blank grids are surrounded by grids with relatively small R_g values (Figure S6), consistent with the idea that these regions are less accessible to probes. While AFM measurements on the dry PDMAEA brush show a smooth surface with a roughness of

0.3 nm (Figure S3), the local surface morphology of the brush changes upon swelling. Previous studies[44 45] for solvated PEBs using *in-situ* AFM measurements also found domains of the rough surface whose characteristic length scale is at the micron level, similar to the apparent scale in our system. These prior studies, however, were not able to use AFM to quantify the spatial heterogeneity within the brush. Thus, 3D single-molecule tracking data provide a route to quantify the effects of spatial heterogeneity using probe motion inside the polymer brush.

Confined probes move faster axially than laterally, whereas the opposite trend is observed for the unconfined probe population. A scatter plot showing the R_g calculated in the x-y plane vs. the z-axis compares the correlation of motion in the lateral (x-y) and axial (z) directions, with the colormap showing the data density (Figure 5a). Two distinct and slightly overlapping populations of probes are clearly evident, separated by the dark line between the two regions. By examining the trajectories from each population (Figure S8, 9), we found them to represent confined (left, shaded in red) and unconfined (right, shaded in grey) populations, respectively.

The confined population consists of 23.4% of the total observed trajectories, with a correlation between axial and lateral dimension, R_{g_z} and R_{g_xy}, of r = 0.85. The correlation in the spatial dimensions suggests that the available space for a confined probe to explore is relatively isotropic. However, a

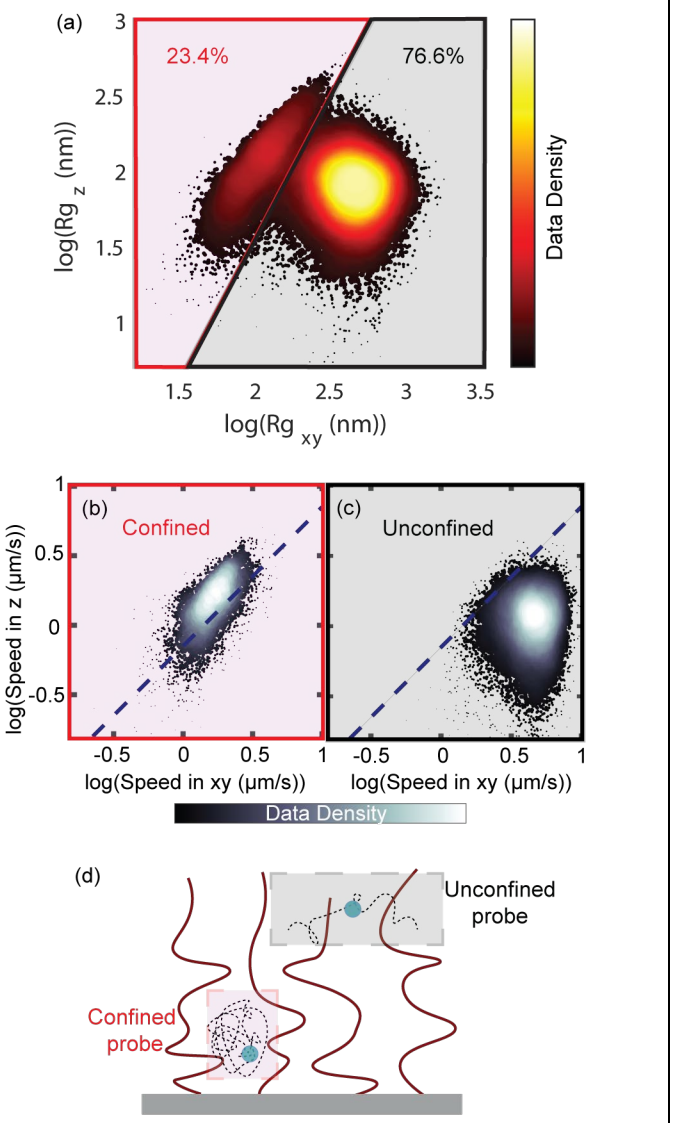

Figure 5 The confined population diffuses faster axially than laterally with the mobility correlated, opposite to the unconfined population. (a) A scatter plot showing the correlation between the R_g in the x-y plane and the z-axis. The two shaded regions separate the confined (red) and unconfined (black) populations, containing 23.4% and 76.6% of the trajectories, respectively. 13548 trajectories are used in this plot. (b, c) Scatter plots of the speeds in the x-y plane and z-axis for the confined (b) and unconfined (c) populations. A line of $y = x - \log(\sqrt{2})$ is plotted, showing the theoretical 1:1 correlation with dimensional correction. (d) A carton illustration of proposed probe transport mechanism. The blue spheres represent fluorescence probe.

closer examination shows a biased relationship. Figure 5b compares the apparent speed in each trajectory step in both directions, calculated by the total distance traveled in each frame divided by the total frame time interval, for axial (z) vs. lateral (x-y) displacements; the dashed line represents a 1:1 relationship, which would be expected in an isotropic system. The data in Figure 5b suggests that the confined probes explores space somewhat faster axially than laterally. This asymmetry is consistent with anisotropic structure of PEBs in the axial dimensions. Because the polymer density decreases away from the substrate, probes become less confined towards the brush periphery and are able to move faster there. Interestingly, the electrostatic potential in PEBs also varies along the axial direction but is invariant parallel to the surface[43], which may also influence charge probe motion.

In the unconfined population, representing 76.6% of trajectories, there is no correlation (r = 0.06) between axial and lateral motion. MSD analysis suggests the lateral motion is Brownian with a diffusion coefficient (D) of $0.476 \pm 0.006\ \mu m^2/s$ whereas the reported D value[41] for the Alexa Fluor 546 molecule in water is 3 orders of magnitude larger. The dynamics of the unconfined probes are slowed down by the charge attraction from polymer chains. However, the speeds in the lateral direction are greater than those in the axial direction (Figure 5c). The axial diffusion of unconfined probes is restricted, as MSD fitting shows the $\alpha = 0.49 < 1$ (Table S1). For this population, the observation of motion along the z-axis is restricted by the height of the PEB. As a probe moves above the brush layer, its diffusion speed increases beyond the range of our observation window. We believe, therefore, that the unconfined population *observed* in our experiments is comprised of dyes

diffusing between chains, biased toward those with limited motion axially. (Detailed calculation is presented in Supporting Information, section 6.)

Although probes in the unconfined population exhibit larger R_g than those in the confined population, Figure 5a suggests that there are striking differences in the space available for lateral and axial diffusion for the two populations. Probes in the observed unconfined population explore a larger lateral space but a smaller axial (z) space than probes in the confined population. Further, the distribution of R_{g_z}, which could be taken as half of the characteristic probe penetration depth, is larger for the confined population than unconfined ones, as shown in Figure 5a. For most confined particles, $2R_{g\_z}$ is comparable to the extended height of the PDMAEA brush at pH 3 (~ 450nm) while $2R_{g\_z}$ for the unconfined population is around 60 – 250 nm. We suggest that this is due to differences in the vertical location of probes in the two populations, such that they experience different average local polymer densities. For weak PEBs, the monomer density profile decays from the substrate to the top layer following a parabolic density profile,[8] with increasing dispersity leading to an extended density profile near the brush surface.[46] Our data is consistent with the view that probes in the unconfined/mobile population primarily access the upper layer of the brush where the distance between chains is larger. The proposed mechanism for the two types of motion and their locations are illustrated in Figure 5d.

Conclusion

We establish 3D single molecule tracking inside a PEB and provide microscopic insight into the complex transport mechanisms, with an upgraded high throughput tracking algorithm. Our results show the PDMAEA brush is spatially heterogeneous on the micron length scale, which leads to distinct distributions of confined and unconfined motions of probes within the brush. Confined probes favor motion in the axial directions, whereas observed unconfined probes preferentially move in the lateral direction, suggesting that these mobile probes access regions of lower polymer density within the brush, and those regions are predominantly near the brush periphery. The experimental platform and analysis methods developed in this work can be widely applied to resolve microscopic molecule transport mechanisms and structural information in complex anisotropic systems. We suggest that the analytical tools and insight presented here will motivate further study of solute transport in a wide range of polyelectrolyte brushes. In the future, we will further look into the transport in PEB under tunable conformation changes.

Supporting Information. Materials preparation, synthesis schematic, probe transport at different pH conditions, XPS and AFM characterizations, grafting density characterization, MSD analysis details, heatmap analysis of R_g values, neighbors of blank regions on the R_g heatmap analysis, trajectory lengths dependence analysis, trajectory classification details, trajectory length filter analysis.

Acknowledgment

C.F.L. acknowledges support from the Welch Foundation (Grant No. C-1787) and Kenneth S. Pitzer-Schlumberger Chair in Chemistry. A.B.M. acknowledges support from the National Science Foundation (NSF-CBET, Award No. 2113767). JCC and FS acknowledge support from the National Science Foundation (CBET-2113769) and the Welch Foundation (E-1869). The work was conducted, in part, using resources of the Shared Equipment Authority (SEA) at Rice University.

Author Email Addresses

Dongyu Fan: df24@rice.edu

Shahryar Ramezani Bajgiran: sr72@rice.edu

Farshad Safi Samghabadi: fsamghabadi@uh.edu

Chayan Dutta: cdutta@gsu.edu

Emil Gillett: eng2@rice.edu

Peter J. Rossky: peter.rossky@rice.edu

Jacinta C. Conrad: jcconrad@uh.edu

Amanda B. Marciel: am152@rice.edu

Christy F. Landes: cflandes@rice.edu

References

(1) Wang, S. Q.; Jing, B. X.; Zhu, Y. X. Molecule Motion at Polymer Brush Interfaces from Single-Molecule Experimental Perspectives. *Journal of Polymer Science Part B-Polymer Physics* **2014**, *52* (2), 85-103. DOI: 10.1002/polb.23414.

(2) Conrad, J. C.; Robertson, M. L. Towards mimicking biological function with responsive surface-grafted polymer brushes. *Current Opinion in Solid State & Materials Science* **2019**, *23* (1), 1-12, Review. DOI: 10.1016/j.cossms.2018.09.004.

(3) Zhang, P.; Yang, J. H.; Li, W. C.; Wang, W.; Liu, C. J.; Griffith, M.; Liu, W. G. Cationic polymer brush grafted-nanodiamond via atom transfer radical polymerization for enhanced gene delivery and bioimaging. *Journal of Materials Chemistry* **2011**, *21* (21), 7755-7764, Article. DOI: 10.1039/c1jm10813a.

(4) Yang, W.; Xue, H.; Li, W.; Zhang, J. L.; Jiang, S. Y. Pursuing "Zero" Protein Adsorption of Poly(carboxybetaine) from Undiluted Blood Serum and Plasma. *Langmuir* **2009**, *25* (19), 11911-11916, Article. DOI: 10.1021/la9015788.

(5) Yu, Q.; Cho, J.; Shivapooja, P.; Ista, L. K.; Lopez, G. P. Nanopatterned Smart Polymer Surfaces for Controlled Attachment, Killing, and Release of Bacteria. *Acs Applied Materials & Interfaces* **2013**, *5* (19), 9295-9304, Article. DOI: 10.1021/am4022279.

(6) Nagase, K.; Kobayashi, J.; Kikuchi, A.; Akiyama, Y.; Kanazawa, H.; Okano, T. Monolithic Silica Rods Grafted with Thermoresponsive Anionic Polymer Brushes for High-Speed Separation of Basic Biomolecules and Peptides. *Biomacromolecules* **2014**, *15* (4), 1204-1215, Article. DOI: 10.1021/bm401779r.

(7) Rauch, S.; Uhlmann, P.; Eichhorn, K. J. In situ spectroscopic ellipsometry of pH-responsive polymer brushes on gold substrates. *Analytical and Bioanalytical Chemistry* **2013**, *405* (28), 9061-9069, Article. DOI: 10.1007/s00216-013-7090-z.

(8) Willott, J. D.; Murdoch, T. J.; Webber, G. B.; Wanless, E. J. Physicochemical behaviour of cationic polyelectrolyte brushes. *Progress in Polymer Science* **2017**, *64*, 52-75, Review. DOI: 10.1016/j.progpolymsci.2016.09.010.

(9) Milner, S. T. Polymer Brushes. *Science* **1991**, *251* (4996), 905-914, Article. DOI: 10.1126/science.251.4996.905.

(10) Zhulina, E. B.; Birshtein, T. M.; Borisov, O. V. Theory of Ionizable Polymer Brushes. *Macromolecules* **1995**, *28* (5), 1491-1499, Article. DOI: 10.1021/ma00109a021.

(11) Israels, R.; Leermakers, F. A. M.; Fleer, G. J.; Zhulina, E. B. Charged Polymeric Brushes - Structure and Scaling Relations. *Macromolecules* **1994**, *27* (12), 3249-3261, Article. DOI: 10.1021/ma00090a018.

(12) Mahalik, J. P.; Yang, Y.; Deodhar, C.; Ankner, J. F.; Lokitz, B. S.; Kilbey Ii, S. M.; Sumpter, B. G.; Kumar, R. Monomer volume fraction profiles in pH responsive planar polyelectrolyte brushes. *Journal of Polymer Science Part B: Polymer Physics* **2016**, *54* (10), 956-964, Article. DOI: https://doi.org/10.1002/polb.24008 (acccessed 2021/11/29).

(13) Moglianetti, M.; Webster, J. R. P.; Edmondson, S.; Armes, S. P.; Titmuss, S. Neutron Reflectivity Study of the Structure of pH-Responsive Polymer Brushes Grown from a Macroinitiator at the Sapphire-Water Interface. *Langmuir* **2010**, *26* (15), 12684-12689, Article. DOI: 10.1021/la101550w.

(14) Wetzler, S. P.; Miller, K. A.; Kisley, L.; Stanton, A. L. D.; Braun, P. V.; Bailey, R. C. Real-Time Measurement of Polymer Brush Dynamics Using Silicon Photonic Microring Resonators: Analyte

Partitioning and Interior Brush Kinetics. *Langmuir* **2020**, *36* (35), 10351-10360. DOI: 10.1021/acs.langmuir.0c01336.

(15) Mendivelso-Perez, D. L.; Farooq, M. Q.; Santra, K.; Anderson, J. L.; Petrich, J. W.; Smith, E. A. Diffusional Dynamics of Tetraalkylphosphonium Ionic Liquid Films Measured by Fluorescence Correlation Spectroscopy. *J Phys Chem B* **2019**, *123* (23), 4943-4949. DOI: 10.1021/acs.jpcb.9b01476.

(16) Daniels, C. R.; Reznik, C.; Kilmer, R.; Felipe, M. J.; Tria, M. C. R.; Kourentzi, K.; Chen, W. H.; Advincula, R. C.; Willson, R. C.; Landes, C. F. Permeability of anti-fouling PEGylated surfaces probed by fluorescence correlation spectroscopy. *Colloids and Surfaces B-Biointerfaces* **2011**, *88* (1), 31-38, Article. DOI: 10.1016/j.colsurfb.2011.05.044.

(17) Zhang, Z. J.; Edmondson, S.; Mears, M.; Madsen, J.; Armes, S. P.; Leggett, G. J.; Geoghegan, M. Blob Size Controls Diffusion of Free Polymer in a Chemically Identical Brush in Semidilute Solution. *Macromolecules* **2018**, *51* (16), 6312-6317, Article. DOI: 10.1021/acs.macromol.8b01193.

(18) Zhang, C. F.; Chu, X.; Zheng, Z. L.; Jia, P. X.; Zhao, J. Diffusion of Ionic Fluorescent Probes atop Polyelectrolyte Brushes. *Journal of Physical Chemistry B* **2011**, *115* (51), 15167-15173, Article. DOI: 10.1021/jp204612u.

(19) Reznik, C.; Landes, C. F. Transport in Supported Polyelectrolyte Brushes. *Accounts of Chemical Research* **2012**, *45* (11), 1927-1935, Review. DOI: 10.1021/ar3001537.

(20) Wang, H.; Cheng, L.; Saez, A. E.; Pemberton, J. E. Flow Field Penetration in Thin Nanoporous Polymer Films under Laminar Flow by Forster Resonance Energy Transfer Coupled with Total Internal Reflectance Fluorescence Microscopy. *Analytical Chemistry* **2015**, *87* (23), 11746-11754, Article. DOI: 10.1021/acs.analchem.5b03751.

(21) Marruecos, D. F.; Kastantin, M.; Schwartz, D. K.; Kaar, J. L. Dense Poly(ethylene glycol) Brushes Reduce Adsorption and Stabilize the Unfolded Conformation of Fibronectin. *Biomacromolecules* **2016**, *17* (3), 1017-1025, Article. DOI: 10.1021/acs.biomac.5b01657.

(22) Elliott, L. C. C.; Barhoum, M.; Harris, J. M.; Bohn, P. W. Single Molecule Tracking Studies of Lower Critical Solution Temperature Transition Behavior in Poly(N-isopropylacrylamide). *Langmuir* **2011**, *27* (17), 11037-11043, Article. DOI: 10.1021/la201753v.

(23) Chen, T. Y.; Jung, W.; Santiago, A. G.; Yang, F.; Krzeminski, L.; Chen, P. Quantifying Multistate Cytoplasmic Molecular Diffusion in Bacterial Cells via Inverse Transform of Confined Displacement Distribution. *J Phys Chem B* **2015**, *119* (45), 14451-14459. DOI: 10.1021/acs.jpcb.5b08654.

(24) Chan, J. M.; Kordon, A. C.; Zhang, R.; Wang, M. Direct visualization of bottlebrush polymer conformations in the solid state. *Proc Natl Acad Sci U S A* **2021**, *118* (40), e2109534118. DOI: 10.1073/pnas.2109534118.

(25) Pavani, S. R. P.; Thompson, M. A.; Biteen, J. S.; Lord, S. J.; Liu, N.; Twieg, R. J.; Piestun, R.; Moerner, W. E. Three-dimensional, single-molecule fluorescence imaging beyond the diffraction limit by using a double-helix point spread function. *Proceedings of the National Academy of Sciences of the United States of America* **2009**, *106* (9), 2995-2999, Article. DOI: 10.1073/pnas.0900245106.

(26) Alvarez, L. H.; Rudov, A. A.; Gumerov, R. A.; Lenssen, P.; Simon, U.; Potemkin, II; Woll, D. Controlling microgel deformation via deposition method and surface functionalization of solid supports. *Physical Chemistry Chemical Physics* **2021**, *23* (8), 4927-4934, Article. DOI: 10.1039/d0cp06355j.

(27) Zepeda, O. J.; Bishop, L. D. C.; Dutta, C.; Sarkar-Banerjee, S.; Leung, W. W.; Landes, C. F. Untying the Gordian KNOT: Unbiased Single Particle Tracking Using Point Clouds and Adaptive Motion

Analysis. *Journal of Physical Chemistry A* **2021**, *125* (39), 8723-8733, Article. DOI: 10.1021/acs.jpca.1c06100.

(28) Munro, I.; Garcia, E.; Yan, M.; Guldbrand, S.; Kumar, S.; Kwakwa, K.; Dunsby, C.; Neil, M. A. A.; French, P. M. W. Accelerating single molecule localization microscopy through parallel processing on a high-performance computing cluster. *Journal of Microscopy* **2019**, *273* (2), 148-160, Article. DOI: 10.1111/jmi.12772.

(29) Zhang, T.; Du, Y. H.; Muller, F.; Amin, I.; Jordan, R. Surface-initiated Cu(0) mediated controlled radical polymerization (SI-CuCRP) using a copper plate. *Polymer Chemistry* **2015**, *6* (14), 2726-2733. DOI: 10.1039/c5py00093a.

(30) Yan, W. Q.; Fantin, M.; Ramakrishna, S.; Spencer, N. D.; Matyjaszewski, K.; Benetti, E. M. Growing Polymer Brushes from a Variety of Substrates under Ambient Conditions by Cu-0-Mediated Surface-Initiated ATRP. *Acs Applied Materials & Interfaces* **2019**, *11* (30), 27470-27477, Article. DOI: 10.1021/acsami.9b09529.

(31) Zhang, T.; Du, Y. H.; Kalbacova, J.; Schubel, R.; Rodriguez, R. D.; Chen, T.; Zahn, D. R. T.; Jordan, R. Wafer-scale synthesis of defined polymer brushes under ambient conditions. *Polymer Chemistry* **2015**, *6* (47), 8176-8183, Article. DOI: 10.1039/c5py01274k.

(32) Fujiwara, H. *Spectroscopic ellipsometry: principles and applications*; John Wiley & Sons, 2007.

(33) Elliott, L. C. C.; Barhoum, M.; Harris, J. M.; Bohn, P. W. Trajectory analysis of single molecules exhibiting non-Brownian motion. *Physical Chemistry Chemical Physics* **2011**, *13* (10), 4326-4334, Article. DOI: 10.1039/c0cp01805h.

(34) Michalet, X. Mean square displacement analysis of single-particle trajectories with localization error: Brownian motion in an isotropic medium. *Phys Rev E Stat Nonlin Soft Matter Phys* **2010**, *82* (4 Pt 1), 041914. DOI: 10.1103/PhysRevE.82.041914.

(35) Biesalski, M.; Rühe, J.; Johannsmann, D. Segment density profiles of polyelectrolyte brushes determined by Fourier transform ellipsometry. *The Journal of Chemical Physics* **1999**, *111* (15), 7029-7037. DOI: 10.1063/1.480019 (acccessed 2023/03/16).

(36) Biesalski, M.; Johannsmann, D.; Rühe, J. Synthesis and swelling behavior of a weak polyacid brush. *The Journal of Chemical Physics* **2002**, *117* (10), 4988-4994. DOI: 10.1063/1.1490924 (acccessed 2023/03/16).

(37) van de Wetering, P.; Zuidam, N. J.; van Steenbergen, M. J.; van der Houwen, O. A. G. J.; Underberg, W. J. M.; Hennink, W. E. A Mechanistic Study of the Hydrolytic Stability of Poly(2-(dimethylamino)ethyl methacrylate). *Macromolecules* **1998**, *31* (23), 8063-8068. DOI: 10.1021/ma980689g.

(38) Ghasemi, M.; Larson, R. G. Role of electrostatic interactions in charge regulation of weakly dissociating polyacids. *Progress in Polymer Science* **2021**, *112*, 101322. DOI: https://doi.org/10.1016/j.progpolymsci.2020.101322.

(39) Shuang, B.; Wang, W. X.; Shen, H.; Tauzin, L. J.; Flatebo, C.; Chen, J. B.; Moringo, N. A.; Bishop, L. D. C.; Kelly, K. F.; Landes, C. F. Generalized recovery algorithm for 3D super-resolution microscopy using rotating point spread functions. *Scientific Reports* **2016**, *6*, 9, Article. DOI: 10.1038/srep30826.

(40) Reznik, C.; Estillore, N.; Advincula, R. C.; Landes, C. F. Single Molecule Spectroscopy Reveals Heterogeneous Transport Mechanisms for Molecular Ions in a Polyelectrolyte Polymer Brush. *Journal of Physical Chemistry B* **2009**, *113* (44), 14611-14618, Article. DOI: 10.1021/jp906487j.

(41) Petrasek, Z.; Schwille, P. Precise measurement of diffusion coefficients using scanning fluorescence correlation spectroscopy. *Biophysical Journal* **2008**, *94* (4), 1437-1448, Article. DOI: 10.1529/biophysj.107.108811.

(42) Bruce, N. J.; Ganotra, G. K.; Kokh, D. B.; Sadiq, S. K.; Wade, R. C. New approaches for computing ligand–receptor binding kinetics. *Current Opinion in Structural Biology* **2018**, *49*, 1-10. DOI: https://doi.org/10.1016/j.sbi.2017.10.001.

(43) Zhulina, E. B.; Borisov, O. V. Poisson-Boltzmann theory of pH-sensitive (annealing) polyelectrolyte brush. *Langmuir* **2011**, *27* (17), 10615-10633. DOI: 10.1021/la201456a.

(44) Yenice, Z.; Schoen, S.; Bildirir, H.; Genzer, J.; von Klitzing, R. Thermoresponsive PDMAEMA Brushes: Effect of Gold Nanoparticle Deposition. *Journal of Physical Chemistry B* **2015**, *119* (32), 10348-10358, Article. DOI: 10.1021/acs.jpcb.5b04757.

(45) Wang, H.; Pemberton, J. E. Effect of Solvent Quality on Laminar Slip Flow Penetration of Poly(N-isopropylacrylamide) Films with an Exploration of the Mass Transport Mechanism. *Langmuir* **2017**, *33* (30), 7468-7478. DOI: 10.1021/acs.langmuir.7b01598.

(46) de Vos, W. M.; Leermakers, F. A. M. Modeling the structure of a polydisperse polymer brush. *Polymer* **2009**, *50* (1), 305-316, Article. DOI: 10.1016/j.polymer.2008.10.025.

Table of Content Figure